ISSN 1023-1935, Russian Journal of Electrochemistry, 2019, Vol. 55, No. 5, pp. 351–357. © Pleiades Publishing, Ltd., 2019.
Published in Russian in Elektrokhimiya, 2019, Vol. 55, No. 5, pp. 515–522.

Porous $LiMn_2O_4$ Nano-Microspheres as Durable High Power Cathode Materials for Lithium Ion Batteries[1]

Xiaoling Cui[a, b, c], Huixia Feng[a, b, c, *], Jinliang Liu[c], Fengjuan Tang[c], and Hongliang Li[c]

[a] *State Key Laboratory of Advanced Processing and Recycling of Nonferrous Metals, Lanzhou University of Technology, Lanzhou, 730050 China*

[b] *School of Materials Science and Engineering, Lanzhou University of Technology, Lanzhou, 730050 China*

[c] *College of Petrochemical Technology, Lanzhou University of Technology, Lanzhou, 730050 China*

**e-mail: judylut@gmail.com*

Received April 21, 2017; revised November 9, 2017; accepted November 9, 2017

Abstract—Porous $LiMn_2O_4$ spheres was easily fabricated with $MnCO_3$ spheres and MnO_2 as precursors and characterized in terms of structure and performance as the cathode of a lithium ion battery. The presence of pores with the average size of about 50 nm throughout the whole $LiMn_2O_4$ microspheres was confirmed by scanning electron microscope (SEM) and N_2 adsorption–desorption measurements. The electrochemical tests show that the synthesized product has smaller electrochemical polarization, faster Li-ion intercalation kinetics and higher electrochemical stability. It exhibits excellent rate capability and cyclic stability: delivering a reversible discharge capacity of 71 mA h g^{-1} at a 5 C rate and yielding a capacity retention of over 92% at a rate of 0.5 C after 100 cycles. The superior performance of the synthesized product is attributed to its special structure: porous secondary spheres particles consisting of primary single-crystalline nanoparticles. The nanoparticle reduces the path of Li-ion diffusion and increases the reaction sites for lithium insertion/extraction, the pores provide room to buffer the volume changes during charge–discharge and the single crystalline nanoparticle endows the spinel with the best stability. Taking the excellent electrochemical performance and facile synthesis into consideration, the presented porous $LiMn_2O_4$ spheres could be a competitive candidate cathode material for high-performance lithium-ion batteries.

Keywords: lithium manganese oxide, cathode, porous spheres structure, lithium-ion battery

DOI: 10.1134/S1023193519040037

INTRODUCTION

Lithium-ion batteries are widely used in electronic devices such as cell phones, digital cameras and laptops, because of their high energy density and excellent cycling performance, but they are expensive for large-scale applications such as power sources in electric vehicles, compared to lead acid batteries [1, 2]. Spinel $LiMn_2O_4$, because of its low cost and environmental friendliness, is regarded as one of the most promising cathode materials for the next generation of lithium ion batteries [3–5]. However, $LiMn_2O_4$ presents capacity decay and poor cycling stability because of the manganese dissolution and the Jahn–Teller distortion [6–9]. Doping [10–12] and coating [13–15] have been used to improve the stability of $LiMn_2O_4$, but these strategies are at the expense of a loss of capacity.

Other approaches to enhance the performance of $LiMn_2O_4$ cathode have recently focused on reducing the particle size to nanoscale [16–18]. Nanoparticles provide a reduced distance for Li^+ ion diffusion in bulk $LiMn_2O_4$ and increase surface contact area with the electrolyte for electron transfer, leading to an improved rate capability. However, the inferior packing of nanoparticles would lead to lower volumetric energy densities unless special compaction methods are developed [19].

Recently, controlled crystallization method has been used to synthesize $LiMn_2O_4$ spinel microspheres [20]. In general, the $LiMn_2O_4$ powder composed of spherical particles could lead to a higher tap density due to their close package, which would enhance the volumetric energy density compared with the irregularly shaped nanoparticles [21]. However, the solid sphere has very long ion and electron transportation paths compared with nanoparticles because the elec-

[1] The article is published in the original.

trolytes cannot easily penetrate into the internal surface of the solid spheres. Therefore, the cathode material with a porous microsphere consisted of nanocrystallites tightly compacted to form three-dimensional electronic and ionic channels should be an ideal structure [22]. The pores provide room to accommodate the structural strain resulting from repeated Li^+ ion insertion/extraction processes and releases the lattice stress caused by Jahn–Teller distortion during cycling, leading to the improved cyclic stability.

Guo et al. used a novel self-supporting template approach to prepare solid sphere spinel $LiMn_2O_4$ with a tap–density as high as 2.67 g cm^{-3}. But the precursor Mn_3O_4 was prepared by hydrothermal method and sintered at a higher temperature with 1100°C. This process is not convenient for industrial applications [23]. In this work, we report on porous $LiMn_2O_4$ spheres assembled by nanocrystallites with a simple precipitation method as the cathode material for rechargeable lithium batteries. X-ray diffraction (XRD), SEM and N_2 adsorption–desorption measurement were employed to characterize its structure. Significantly, without cation doping or surface coating, the synthesized $LiMn_2O_4$ product used as cathode material is expected to exhibit better electrochemical performances because of porous structure, such as an excellent high-rate capability and a long-term cyclic property. So we applied electrochemical measurements to confirm and explain these performances.

EXPERIMENTAL

The preparation of porous $LiMn_2O_4$ spheres follows a three steps route. First, spherical $MnCO_3$ and $Mn(OH)_2$ was produced by a simple precipitation method using analytical $Mn(Ac)_2 \cdot 4H_2O$ as the manganese source, Na_2CO_3–NaOH (8 : 1 by molar mass) as the precipitants. $Mn(Ac)_2 \cdot 4H_2O$ (0.04 mol L^{-1}) and Na_2CO_3–NaOH (0.045 mol L^{-1}) were dissolved in the distilled water, separately. Then, both solutions was heated to 90°C with stirring. After the complete dispersion of $Mn(Ac)_2$ and Na_2CO_3–NaOH solution, the Na_2CO_3–NaOH solution was added to the $Mn(Ac)_2$ solution. And the solution would turn into milky white, which indicated the initial formation of $MnCO_3$ sphere and $Mn(OH)_2$. Second, 20 mL of H_2O_2 (30 wt %) was added to this milky white solution, a black solution with a high oxidation state of manganese ions would be obtained. Allow the mixture obtained for 3 h and the powders obtained were leached and washed by distilled water several times and then dried in the air at 120°C for 24 h. Third, the mixtures of $MnCO_3$, MnO_2 and $LiNO_3$ with molar ratio of 2 : 1.05 (Mn : Li) were suitably ground in the agate mortar using ethanol as the disperse agent, and dried at 80°C, finally sintered at 700°C for 10 h with a heating rate of 5°C min^{-1} in the air, so the porous $LiMn_2O_4$ spheres (denoted as PS-$LiMn_2O_4$) were achieved. For comparison, the aggregated $LiMn_2O_4$ spheres (denoted as AS-$LiMn_2O_4$) was synthesized by calcination of the mixture of electrolytic manganese dioxide (EMD) and $LiNO_3$ at 700°C for 10 h.

The morphology of the materials was observed by scanning electron microscopy (SEM, JSM-5600, Japan) and transmission electron microscopy (TEM, FEI Tecnai G2 F20). The crystal structures of the samples were analyzed by X-ray diffraction (XRD, Rigaku, D/Max-2400) with CuK_α radiation (40 kV, 150 mA, step size = 0.02°/s). The pore size distribution was determined with Brunauer–Emmett–Teller (BET, Micromeritics ASAP 2020 M) at the temperature of liquid nitrogen (77 K).

The electrode for electrochemical tests was prepared by mixing 84 wt % of active material with 8 wt % of acetylene black and 8 wt % of polyvinylidene difluoride (PVDF) binder. These materials were dispersed in 1-methyl-2-pyrrolidinone (NMP), and the resultant slurry was coated onto an aluminum foil which was used as the counter electrode during the electrochemical measurements. ACR2032 coin cell was used and assembled in an Ar-filled glove box by using the prepared electrode as the cathode, the lithium film as the anode, Celgard 2400 as a separator and 1.0 mol L^{-1} $LiPF_6$ in ethylene carbonate (EC)/diethyl carbonate (DMC) (1 : 1 by volume) as electrolyte.

A charge/discharge test was performed using a Landt cell test system (Landt CT2001A, Wuhan, China). Cells were cycled between 3.5 and 4.3 V (vs. Li/Li^+) at 25°C. Electrochemical impedance spectroscopy (EIS) spectra of the positive electrode were measured in three-electrode cells (the negative and positive electrodes were respectively used as working electrodes and lithium sheets were used both as counter electrode and reference electrode) through CHI660C electrochemical analyzer (Shanghai, China). The impedance measurements were respectively tested at the fully delithiated state of 4.3 V for $LiMn_2O_4$/Li half cells. A sinusoidal AC perturbation of 5 mV was applied to every electrode over the frequency range of 100 kHz to 10 mHz.

RESULTS AND DISCUSSION

Figure 1 gives the SEM images (a)–(d) and selected area electron diffraction (SAED) pattern (g) of PS-$LiMn_2O_4$ sample, and the SEM images of AS-$LiMn_2O_4$ (Figs. 1e and 1f) as comparisons. The low magnification SEM image (Fig. 1a) indicates that the product is composed of homogenous spheres with an average diameter of 750 nm (Fig. 1b), which are obviously inherited from the precursor $MnCO_3$. Figure 1c demonstrates that the $LiMn_2O_4$ spheres are porous and architected with the primary nanoparticles of 200 nm. Meanwhile, the SAED pattern of PS-$LiMn_2O_4$ shows

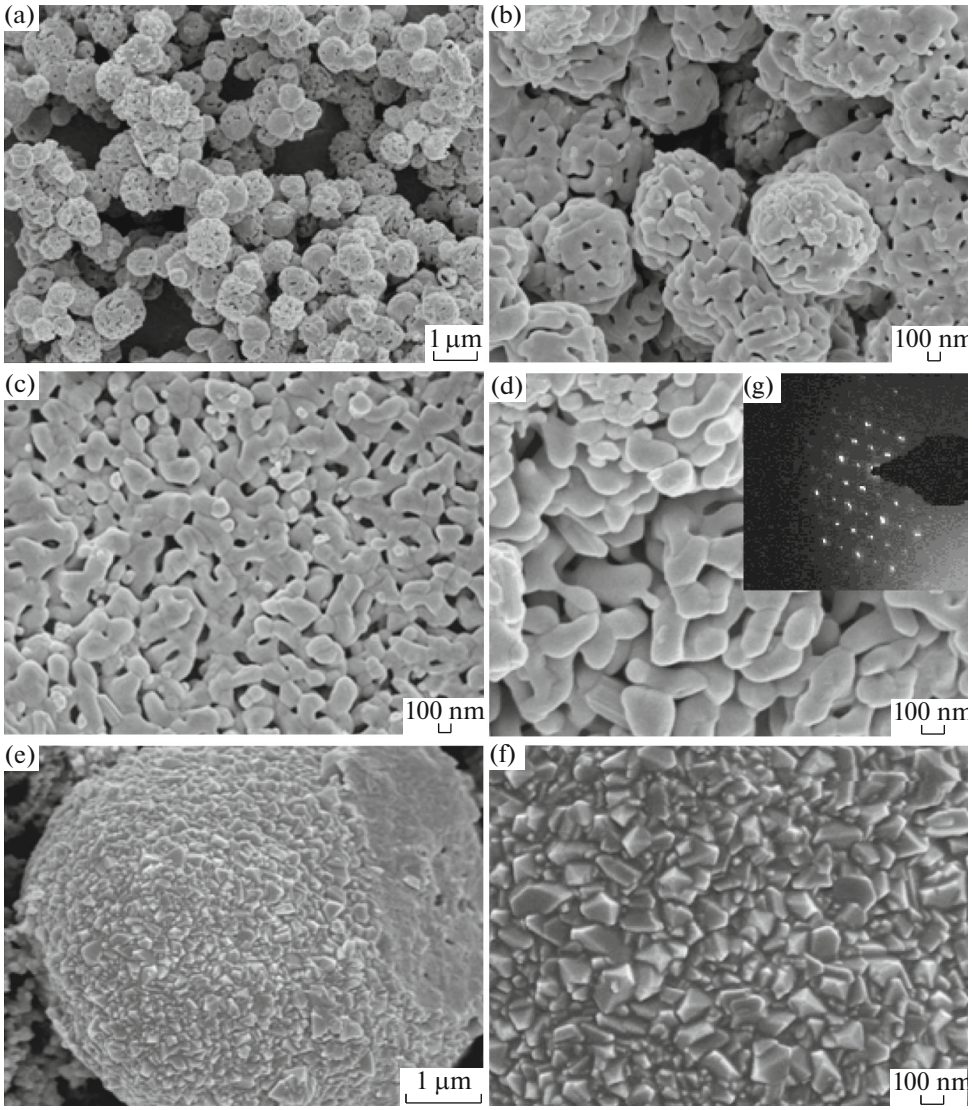

Fig. 1. SEM images (a–d) and SAED pattern (g) of PS-$LiMn_2O_4$, and SEM images (e and f) of AS-$LiMn_2O_4$.

that all of the diffraction point are centrosymmetry which is the strong evidence of single crystal nanomaterials. The cross profile image of a broken sphere in Fig. 1d further reveals that there are abundant pores distributed throughout the interior of the $LiMn_2O_4$ sphere, constructing three-dimensional interconnected channels. As shown in Figs. 1e and 1f, the AS-$LiMn_2O_4$ powders are packed with irregular agglomerates with the particle size of about 250 nm.

XRD patterns of the as prepared cathode are shown in Fig. 2. The diffraction peaks index well to the cubic spinel $LiMn_2O_4$ structure (JCPDS no. 35-0782, *Fd*3*m*, space group 227). According to XRD data, we calculate the cell parameter of porous $LiMn_2O_4$ is a = 8.25124 Å and its tap density is about 1.79 g cm^{-3}. The results are in good agreement with the relative values from literatures [24, 25]. The sharp and strong XRD peaks also demonstrate the good crystallinity and high purity of the products. It indicates the successful preparation of pure phase $LiMn_2O_4$ powders with $MnCO_3$ spheres and MnO_2 as precursors as conventional solid-state reaction method. From Fig. 2 can also be seen that the predominant *hkl* planes such as 111, 311, 400 are those that possess higher thermodynamic stability which clearly indicates that the crystal habit of $LiMn_2O_4$ prepared by this method is more stable [26].

To determine the pore-size distribution and Brunauer–Emmett–Teller (BET) surface area, we measure the adsorption and desorption isotherms of the PS-$LiMn_2O_4$ sample. Figure 3 shows their N_2 adsorption–desorption isotherm and the pore size

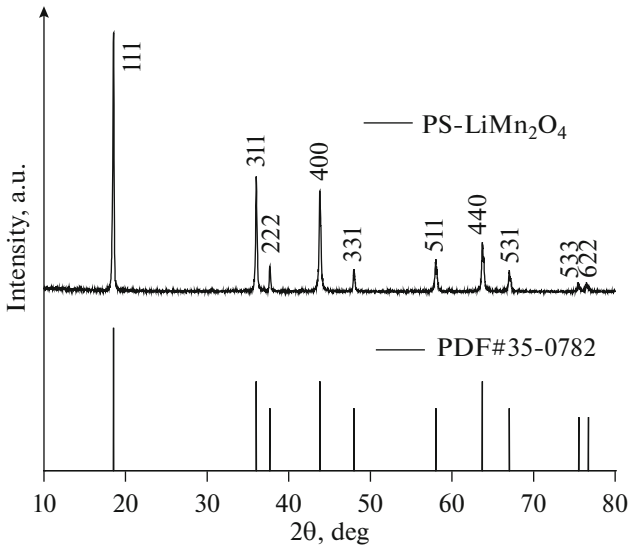

Fig. 2. The XRD pattern of the PS-$LiMn_2O_4$.

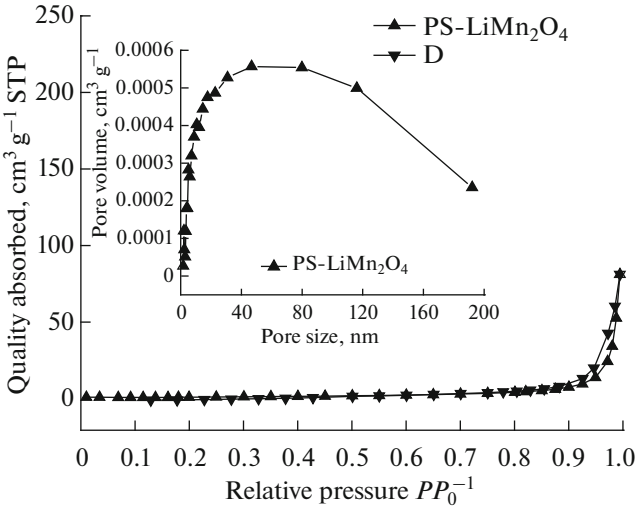

Fig. 3. Nitrogen adsorption/desorption isotherm and Barrette–Joynere–Halenda (BJH) pore size distribution plot (inset) of PS-$LiMn_2O_4$.

distribution curve (inset). For porous PS-$LiMn_2O_4$, the BET surface area is about 5.46 $m^2 g^{-1}$ and the BJH average pore diameter is about 50 nm. In addition, curves indicate the abundance of mesopores in porous PS-$LiMn_2O_4$, which is in good agreement with those observed in SEM image. The data implies that the porous $LiMn_2O_4$ spheres possess a high contact area with the electrolyte and hence a high lithium-ion flux across the interface [27].

The electrochemical performance of porous $LiMn_2O_4$ spheres is discussed as a cathode material for a lithium-ion rechargeable battery. Figure 4a shows the typical charge–discharge profile of the PS-$LiMn_2O_4$ and AS-$LiMn_2O_4$ at 0.1 C between 3.5 and 4.3 V. Both the charge and discharge curves clearly show two-step flat voltage plateaus based on the two different lithium ion's insertion (or extraction) processes [28]. One corresponds to the extraction of Li ions from half of the tetrahedral sites under Li–Li interaction and the other to the extraction from the other half of the tetrahedral sites without Li–Li interaction [29–32]. The potential difference of about 100 mV between these two extraction processes results from the repulsion between Li-ions [32, 33]. At 0.1 C (1 C = 148 mAh g^{-1}) between 3.5 to 4.3 V, the initial discharge specific capacities of PS-$LiMn_2O_4$ cathode and AS-$LiMn_2O_4$ cathode are 138.7 and 130.9 mA h g^{-1}, respectively.

To further illuminate discharge potentials, Fig. 4b reveals the differential capacity (dQ/dV vs. cell's potential) profiles that are derived from the galvanostatic discharging curve. These two peaks can be observed corresponding to the two plateaus in the discharge curves in Fig. 4b. The discharge potentials of PS-$LiMn_2O_4$/Li cell are 3.90 and 4.06 V respectively and those of AS-$LiMn_2O_4$/Li cell are 3.78 and 3.98 V for 0.1 C, respectively. From Fig. 4b, we can find obviously that the average discharge plateaus of PS-$LiMn_2O_4$/Li cell are higher than that of AS-$LiMn_2O_4$/Li cell. Moreover, the capacity percentage at 4.06 V discharge plateau for PS-$LiMn_2O_4$/Li cell is 69.5%, and the capacity percentage at 3.98 V discharge plateau for PS-$LiMn_2O_4$/Li cell is 29.6%. We can conclude that PS-$LiMn_2O_4$/Li cell has smaller electrochemical polarization. That is to say, compared with AS-$LiMn_2O_4$, PS-$LiMn_2O_4$ can provide higher working voltage, and is more attractive for use in large energy storage systems needing high power density, such as electric vehicles (EVs) and hybrid electric vehicles (HEVs).

Figure 4c compares the rate capability of the PS-$LiMn_2O_4$ and AS-$LiMn_2O_4$ with charge/discharge rates of 0.2 to 5 C. PS-$LiMn_2O_4$ shows obviously slower capacity decay with increasing discharge rates. It presents a slowly declining trend up to 5 C, reaching a discharge capacity of 71 mA h g^{-1}. On the contrary, the capacity of AS-$LiMn_2O_4$ is found to decay quickly at high discharge rate, it is only 47 mA h g^{-1} at 5 C. After 20 cycles with discharge rate constantly changing, the discharge capacity of PS-$LiMn_2O_4$ is still maintained 113 mA h g^{-1} when the rate comes back to 0.5 C; however, AS-$LiMn_2O_4$ shows a capacity of only 108 mA h g^{-1} at the same rate. The good capacity retention for PS-$LiMn_2O_4$ after cycling at constantly changing discharge rate suggests that its structure is stable. Evidently, the excellent rate capability is due to abundant porous structure and high active surface area. The pores allow the electrolyte to enter and

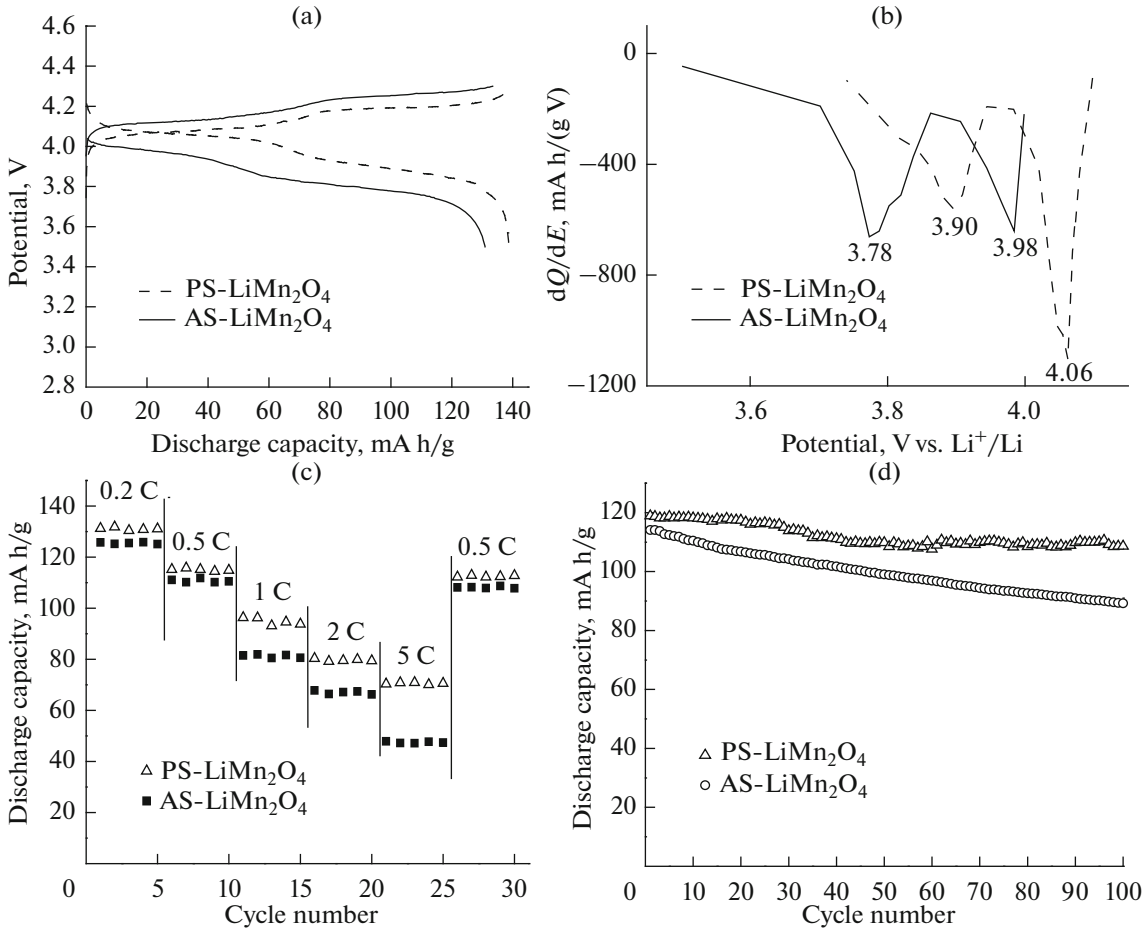

Fig. 4. Electrochemical performance of PS-$LiMn_2O_4$ and AS-$LiMn_2O_4$: (a) initial charge–discharge curves at 0.1 C; (b) deferential capacity profiles at 0.1 C; (c) rate capability; (d) cycle performance at room temperature at 0.5 C.

increase the contact surface area between the nanoparticles and the electrolyte for lithium insertion/extraction, and the nanosize of the particles reduces the path of the Li ion diffusion inside the particles. Such behavior coincides with consequence of SEM and BET analysis.

Figure 4d reveals the cycle performance of the PS-$LiMn_2O_4$ and AS-$LiMn_2O_4$ at 0.5 C rate. After 100 cycles at 0.5 C rate, the discharge capacity of the PS-$LiMn_2O_4$ is still maintained 92% of its capacity compared with first cycle, which is much higher than 78% of the AS-$LiMn_2O_4$ capacity maintained. The excellent cyclic stability of the PS-$LiMn_2O_4$ is attributed to its special architecture. The interior space in the spheres can accommodate the volume change during lithium insertion/extraction processes and can release the lattice stress caused by Jahn–Teller distortion during cycling, while the single-crystalline provides the best structure stability.

Figure 5 shows the electrochemical impedance spectra (EIS) of the batteries with different samples as electrodes at the fully delithiated state of 4.3 V (the cut-off voltage of the charge process for $LiMn_2O_4$/Li cells).The plot includes the real component of the impedance on the horizontall axis (Z'), and the imaginary component of the impedance on the vertical axis (Z'').

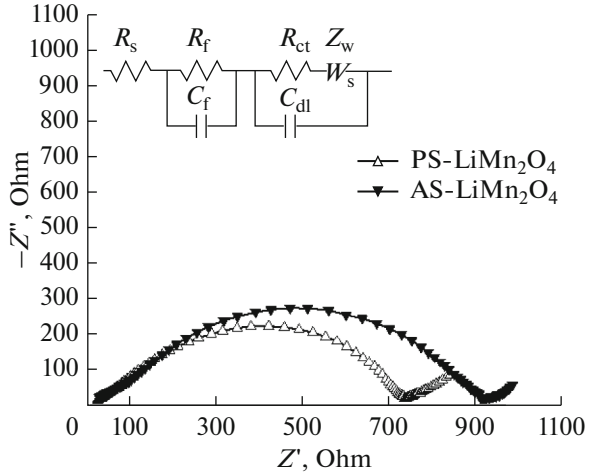

Fig. 5. EIS spectra of the PS-$LiMn_2O_4$ and AS-$LiMn_2O_4$ in the frequency range between 0.01 Hz and 100 kHz.

The EIS spectrums are combination of the depressed semicircle at high-to-middle frequency region and an inclined line in the low frequency region. The intercept at the Z' axis corresponds to the ohmic resistance (R_s), the semicircle is related losely to the lithium-ion migration resistance (R_f) through the multilayer surface films and the charge transfer resistance (R_{ct}) in high-to-middle frequency range. Apparently, it can be seen from Fig. 5 that R_{ct} of the PS-$LiMn_2O_4$is lower than that of the AS-$LiMn_2O_4$ sample. The higher charge transfer resistance (R_{ct}) of the AS-$LiMn_2O_4$ cell signifies the more capacity loss in the high charge/discharge rate, which is in good agreement with the C-rate capacity data. Furthermore, the inclined line in the low frequency region which is related to the lithium-ion diffusion in the $LiMn_2O_4$ particles represents the Warburg impedance (σ_w) [34]. The following simplified equation [35] were applied to obtain the lithium ion diffusion coefficient D_{Li+}

$$D_{Li^+} = \frac{R^2T^2}{2A^2n^4F^4C_{Li}{}^2\sigma^2},$$

where R means the gas constant ($R = 8.314$ J mol^{-1} K^{-1}), T is the absolute temperature of test environment, A is the area of the cathode material, n is the number of electrochemical reaction electron ($n = 2$ for $LiMn_2O_4$), F is the faraday constant ($F = 96\,500$ C mol^{-1}), C_{Li} is the molar concentration of lithium ion (2.43×10^{-2} mol/cm^3 for spinel), and σ is Warburg resistance factor which can be determined from the measured slope of the real or imaginary part in the low frequency region of the modeling impedance plot plotted against $\omega^{-0.5}$: $Z_{Re} = \sigma\omega^{-0.5}\omega$ ($\omega = 2\pi f$) is the angular frequency.

The D_{Li+} in PS-LMO and AS-LMO calculated by the equation listed above and following Fig. 5 are 1.948×10^{-9} and 1.068×10^{-9} cm^2 s^{-1}, respectively. Consequently, the porous $LiMn_2O_4$ tend to faster Li-ion intercalation kinetics.

The parameters of impedance spectra is simulated and fitted with an equivalent circuit by ZView software as shown in Fig. 5.

CONCLUSIONS

In this paper, we report a porous $LiMn_2O_4$ spheres with excellent rate capability and cyclic stability when used as the cathode of a lithium ion battery. Porous $LiMn_2O_4$ spheres constructed with single-crystalline nanoparticles have successfully been synthesized using $MnCO_3$ spheres and MnO_2 as precursors. The presence of pores with the average size of about 50 nm throughout the whole $LiMn_2O_4$ microspheres and the pore-size distribution were confirmed by SEM and N_2 adsorption–desorption measurements. The charge–discharge tests show that PS-$LiMn_2O_4$/Li cell have smaller electrochemical polarization and can provide higher working voltage. It delivers a reversible discharge capacity of 71 mA h g^{-1} at a rate of 5 C and yields a capacity retention of over 92% at a rate of 0.5 C after 100 cycles. The excellent performance is attributed to the special architecture of the synthesized $LiMn_2O_4$. The nanoparticle reduces the path of the Li ion diffusion and increases the reaction sites for lithium insertion/extraction, and the pores provide space to buffer the volume changes during charge–discharge and the single crystalline endows the spinel with the best stability. Taking the excellent electrochemical performance and facile synthesis into consideration, the presented porous $LiMn_2O_4$ spheres could be a competitive candidate cathode material for high-performance lithium-ion batteries used for electric vehicles (EV) and hybrid electric vehicles (HEV) in the near future.

FUNDING

This work was supported by the Natural Science Foundation of China (nos. 21406100 and 21566021), the Science and Technology Support Project of Gansu Province (no. 144GKCB029).

REFERENCES

1. Farmann, A. and Sauer, D.U., A comprehensive review of on-board State-of-Available-Power prediction techniques for lithium-ion batteries in electric vehicles, *J. Power Sources,* 2016, vol. 329, p. 123.
2. Lin, D., Liu, Y., and Cui, Y., Reviving the lithium metal anode for high-energy batteries, *Nature Nanotech.,* 2017, vol. 12, p. 194.
3. Mao, F.X., Guo, W., and Ma, J.M., Research progress on design strategies, synthesis and performance of $LiMn_2O_4$-based cathodes, *Rsc. Adv.,* 2015, vol. 5, p. 105248.
4. Xu, G., Liu, J., Zhang, C., Cui, G., and Chen, L., Strategies for improving the cyclability and thermo-stability of $LiMn_2O_4$-based batteries at elevated temperatures, *J. Mater. Chem. A,* 2015, vol. 3, p. 4092.
5. Liu, Q.L., Wang, S.P., Tan, H.B., Yang, Z.G., Zeng, J., et al., Preparation and doping mode of doped $LiMn_2O_4$ for Li-ion batteries, *Energies,* 2013, vol. 6, p. 1718.
6. Li, B., Wang, Y., Rong, H., Wang, Y., Liu, J., Xing, L., Xu, M., and Li, W., A novel electrolyte with the ability to form a solid electrolyte interface on the anode and cathode of a $LiMn_2O_4$/graphite battery, *J. Mater. Chem. A,* 2013, vol. 1, p. 12954.
7. Yang, L.D., Xie, J., Cao, G.S., and Zhao, X.B., Single-crystalline $LiMn_2O_4$ nanotubes synthesized via template-engaged reaction as cathodes for high-power lithium ion batteries, *Adv. Funct. Mater.,* 2011, vol. 21, p. 348.
8. Wang, J.G., Jin, D.D., Liu, H.Y., Zhang, C.B., Zhou, R., Shen, C., Xie, K.Y., and Wei, B.Q., All-manganese-

based Li-ion batteries with high rate capability and ultralong cycle life, *Nano Energy,* 2016, vol. 22, p. 524.

9. Lee, S., Cho, Y., Song, H.K., Lee, K.T., and Cho, J., Carbon-coated single-crystal $LiMn_2O_4$ nanoparticle clusters as cathode material for high-energy and high-power lithium-ion batteries, *Angew. Chem. Int. Ed. Engl.,* 2012, vol. 51, p. 8748.
10. Xiong, L., Xu, Y., Tao, T., and Goodenough, J.B., Synthesis and electrochemical characterization of multi-cations doped spinel $LiMn_2O_4$ used for lithium ion batteries, *J. Power Sources,* 2012, vol. 199, p. 214.
11. Dai, K., Mao, J., Li, Z., Zhai, Y.C., Wang, Z.H., Song, X.Y., Battaglia, V., and Liu, G., Microsized single-crystal spinel LAMO for high-power lithium ion batteries synthesized via polyvinylpyrrolidone combustion method, *J. Power Sources,* 2014, vol. 248, p. 22.
12. Jiang, Q.Q., Liu, D.D., Zhang, H., and Wang, S., Plasma-assisted sulfur doping of $LiMn_2O_4$ for high-performance lithium-ion batteries, *J. Phys. Chem. C,* 2015, vol. 119, p. 28776.
13. Zhao, J., Qu, G., Flake, J.C., et al., Low temperature preparation of crystalline ZrO_2 coatings for improved elevated-temperature performances of Li-ion battery cathodes, *Chem. Commun.,* 2012, vol. 48, p. 8108.
14. Zhang, C.C., Liu, X.Y., Su, Q.L., Wu, J.H., Huang, T., and Yu, A.S., Enhancing electrochemical performance of $LiMn_2O_4$ cathode material at elevated temperature by uniform nanosized TiO_2 coating, *ACS Sustain. Chem. Eng.,* 2017, vol. 5, p. 640.
15. Patel, R.L., Park, J., and Liang, X.H., Ionic and electronic conductivities of atomic layer deposition thin film coated lithium ion battery cathode particles, *Rsc. Adv.,* 2016, vol. 6, p. 98768.
16. Yang, G.R., Wang, L., Wang, J.N., and Yan, W., Tailoring the morphology of one-dimensional hollow $LiMn_2O_4$ nanostructures by single-spinneret electrospinning, *Mater. Lett.,* 2016, vol. 177, p. 13.
17. Hung, I.M., Yang, Y.C., Su, H.J., and Zhang, J., Influences of the surfactant on the performance of nano-$LiMn_2O_4$ cathode material for lithium-ion battery, *Ceram. Int.,* 2015, vol. 41, p. S779.
18. Jiang, H., Fu, Y., Hu, Y.J., Yan, C.Y., Zhang, L., Lee, P.S., and Li, C.Z., Hollow $LiMn_2O_4$ nanocones as superior cathode materials for lithium-ion batteries with enhanced power and cycle performances, *Small,* 2014, vol. 10, p. 1096.
19. Wang, F.X., Xiao, S.Y., Zhu, Y.S., Chang, Z., Hu, C.L., Wu, Y.P., and Holze, R., Spinel $LiMn_2O_4$ nanohybrid as high capacitance positive electrode material for supercapacitors, *J. Power Sources,* 2014, vol. 246, p. 19.
20. Li, J., Zhang, X., Peng, R.F., Huang, Y.J., Guo, L., and Qi, Y.C., $LiMn_2O_4$/graphene composites as cathodes with enhanced electrochemical performance for lithium-ion capacitors, *Rsc Adv.,* 2016, vol. 6, p. 54866.
21. Li, S., Wei, X.G., Chang, Z.R., Chen, X.N., Yuan, X.Z., and Wang, H.J., Facile fabrication of $LiMn_2O_4$ microspheres from multi-shell MnO_2 for high-performance lithium-ion batteries, *Mater. Lett.,* 2014, vol. 135, p. 75.
22. Deng, J.Q., Pan, J., Yao, Q.R., Wang, Z.M., and Zhou, H.Y., Porous core-shell $LiMn_2O_4$ microellipsoids as high-performance cathode materials for Li-ion batteries, *J. Power Sources,* 2015, vol. 278, p. 370.
23. Guo, D.L., Chang, Z.R., Tang, H.W., Li, B., Xu, X.H., Yuan, X.Z., and Wang, H.J., Electrochemical performance of solid sphere spinel $LiMn_2O_4$ with high tap density synthesized by porous spherical Mn_3O_4, *Electrochim. Acta,* 2014, vol. 123, p. 254.
24. Zhou, Y.B., Deng, Y.F., Yuan, W.H., and Chen, G.H., Synthesis of spinel $LiMn_2O_4$ microspheres with durable high rate capability, *Trans. Nonferrous Met. Soc.,* 2012, vol. 22, p. 2541.
25. Tang, H., Chang, Z., Zhao, H., Yuan, X.Z., Wang, H.J., and Gao, S.Y., Effects of precursor treatment on the structure and electrochemical properties of spinel $LiMn_2O_4$ cathode, *J. Alloy. Compd.,* 2013, vol. 566, p. 16.
26. Ragavendran, K., Chou, H.L., Lu, L., Lai, M.O., Hwang, B.J., Ravi Kumar, R., Gopukumar, S., Emmanuel, B., Vasudevan, D., and Sherwood, D., Crystal habits of $LiMn_2O_4$ and their influence on the electrochemical performance, *Mater. Sci. Eng. B,* 2011, vol. 176, p. 1257.
27. Arico, A.S., Bruce, P., Scrosati, B., Tarascon, J.M., and Van, S.W., Nanostructured materials for advanced energy conversion and storage devices, *Nat. Mater.,* 2005, vol. 4, p. 366.
28. Ouyang, C., Shi, S., Wang, Z., Huang, X., and Chen, L., Experimental and theoretical studies on dynamic properties of Li ions in $LixMn_2O_4$, *Solid State Commun.,* 2004, vol. 130, p. 501.
29. Sun, W., Cao, F., Liu, Y., Zhao, X., Liu, X., and Yuan, J., Nanoporous $LiMn_2O_4$ nanosheets with exposed {111} facets as cathodes for highly reversible lithium-ion batteries, *J. Mater. Chem.,* 2012, vol. 22, p. 20962.
30. Goodenough, J.B. and Kim, Y., Challenges for rechargeable Li batteries, *Chem. Mater.,* 2010, vol. 22, p. 587.
31. Hosono, E., Kudo, T., Honma, I., Matsuda, H., and Zhou, H., Synthesis of single crystalline spinel $LiMn_2O_4$ nanowires for a lithium ion battery with high power density, *Nano Lett.,* 2009, vol. 9, p. 1045.
32. Goodenough, J.B. and Park, K.S., The Li-ion rechargeable battery: a perspective, *J. Am. Chem. Soc.,* 2013, vol. 135, p. 1167.
33. Ellis, B.L., Lee, K.T., and Nazar, L.F., Positive electrode materials for Li-ion and Li batteries, *Chem. Mater.,* 2010, vol. 22, p. 691.
34. Striebel, K.A., Sakai, E., and Carins, E.J., Impedance studies of the thin film $LiMn_2O_4$/electrolyte interface, *J. Electrochem. Soc.,* 2002, vol. 149, p. A61.
35. Jin, Y.C. and Duh, J.G., Kinetic study of high voltage spinel cathode material in a wide temperature range for lithium ion battery, *J. Electrochem. Soc.,* 2017, vol. 164, p. A735.